

Structure—Activity Relationships of Mineral Dusts as Heterogeneous Nuclei for Ammonium Sulfate Crystallization from Supersaturated Aqueous Solutions

SCOT T. MARTIN,^{*,†} JULIE SCHLENKER,[‡]
J. HOLLY CHELF,[‡] AND
OWEN W. DUCKWORTH[†]

Division of Engineering and Applied Sciences, 29 Oxford Street, Pierce Hall, Room 122, Harvard University, Cambridge, Massachusetts 02138, and Department of Environmental Sciences and Engineering, CB#7400, 112 Rosenau Hall, University of North Carolina at Chapel Hill, Chapel Hill, North Carolina 27599-7400

Mineral inclusions, present in aqueous atmospheric salt droplets, regulate crystallization when relative humidity decreases by providing a surface for heterogeneous nucleation and thus reducing the critical supersaturation. Although laboratory studies have quantified these processes to some extent, the diverse atmospheric mineralogy presents more chemical systems than practically feasible for direct study. Structure—activity relationships are necessary. To that end, in the present work the interactions of ammonium sulfate with corundum, hematite, mullite, rutile, anatase, and baddeleyite were studied by diffuse reflectance fourier transform infrared spectroscopy (DRIFTS) and by epitaxial modeling. The spectroscopic results show that shifts in sulfate peak positions due to chemisorption are not a correlative indicator of the efficacy of heterogeneous nucleation. In contrast, epitaxial modeling results of unreconstructed surfaces explain the sequence of critical supersaturations for constant particle size. If validated by further work, this computer modeling method would provide an important structure—activity tool for the estimation of heterogeneous nucleation properties of the atmospheric mineralogy.

Introduction

A significant source of uncertainty in global climate change models is the quantification of the role of aerosols (1–3). In addition to scattering directly incoming solar radiation, atmospheric particles participate in several indirect processes, such as being cloud condensation nuclei (4) or being the medium for surface and bulk chemical reactions significant enough to affect ozone distribution and sulfur oxidation (5). The physicochemical properties of atmospheric particles are strongly influenced by their phase (6). Dry, small, relatively chemically inert particles occur at lower relative humidities while wet, optically large, chemically active

particles predominant at higher relative humidities. Similarly, aqueous particles are found at warmer temperatures, whereas ice particles form at cooler temperatures. A current challenge is to understand the conditions leading to the transformation from one physical state to another. One synergistic interaction occurs between aqueous salts and mineral dusts. The salts are the receptor of hygroscopic uptake and the portion of the particle undergoing the most physical cycling, whereas the surfaces of mineral dusts incorporated inside the aqueous salt particles provide atomic templates to induce the phase changes (7–8).

Our work thus far has demonstrated that mineral dust constituents are active in promoting the efflorescence (i.e., crystallization) of ammonium sulfate particles. In the absence of mineral inclusions, aqueous ammonium sulfate particles crystallize by homogeneous nucleation at 35% relative humidity (RH) during drying, even though saturation occurs at 79.5% RH (i.e., $\Delta G > 0$ for $RH < 79.5\%$). Expressed as a change in the saturation ratio (S) of the aqueous phase with respect to crystalline $(\text{NH}_4)_2\text{SO}_4$, $S = 1$ for thermodynamic equilibrium and $S = 35$ for homogeneous nucleation. Inclusion of the mineral constituents decreases the supported metastability by opening a channel for heterogeneous nucleation. The effect on S for constant particle diameter is as follows: (A) Mixed anatase and rutile TiO_2 ($S = 4.4$), baddeleyite monoclinic ZrO_2 ($S = 7.0$), and $\delta\text{-Al}_2\text{O}_3$ ($S = 8.2$) (7) and (B) corundum $\alpha\text{-Al}_2\text{O}_3$ ($S = 15.3$), hematite $\alpha\text{-Fe}_2\text{O}_3$ ($S = 16.4$), mullite $\text{Al}_6\text{Si}_2\text{O}_{13}$ ($S = 22.4$), and amorphous silica SiO_2 ($S = 35$) (8). The size classes denoted by A and B are approximately $2\ \mu\text{m}$ and $250\ \text{nm}$. For submicrometer particle diameters, S depends strongly on size (8).

An outstanding question from this work is why some mineral oxides are more active than others. As a subject, heterogeneous nucleation is poorly understood. In the present paper, we test two hypotheses on the differential activities of the employed minerals. In the first hypothesis, we suppose that sulfate chemisorbs to the mineral surface and that the strength of that bond is an indicator of the activity of a mineral. To test the hypothesis, infrared spectra of the sulfato-metal surface complexes are collected by diffuse reflectance infrared spectroscopy (DRIFTS) (9), and the nature of the surface complex is related to the heterogeneous activity of the mineral. Germ formation is believed to proceed by the formation of a metal-sulfato complex by the displacement of surficial -OH (10).

In the second hypothesis, we suppose that, because a crystalline germ grows on the mineral surface, the likelihood of germ formation is quantitatively related to the extent that the germ is a crystalline extension of the substrate, i.e., the goodness of crystallographic match. To test this hypothesis, a modeling approach considers the crystallographic match between unreconstructed surfaces of the minerals and an incipient ammonium sulfate germ (11). Energy terms derived from this modeling are compared to the observed heterogeneous nucleation activities to test for structure—activity relationships. In the long term, quantifying the role of heterogeneous nucleation in the atmosphere requires the development of a comprehensive understanding of structure—activity relationships because the number of minerals in the atmosphere likely exceeds the number of measurements that will be completed in the lab.

Experimental Section

Materials. For the DRIFTS measurements, high surface area mineral particles obtained from Degussa Corp. are employed: baddeleyite monoclinic ZrO_2 , $40\ \text{m}^2/\text{g}$; SiO_2 , $175\text{--}225\ \text{m}^2/\text{g}$;

* Corresponding author phone: (617) 495-7620; fax: (617) 495-9837; E-mail: scot_martin@harvard.edu; Web: <http://www.deas.harvard.edu/~smartin>.

[†] Harvard University.

[‡] University of North Carolina at Chapel Hill.

mixed anatase (80%) and rutile (20%) TiO₂ (P25), 35–65 m²/g; δ-Al₂O₃, 85–115 m²/g (12). A low surface area α-Fe₂O₃ powder (Fisher) is also employed. High surface areas are desirable to obtain a large signal for the sulfato-metal complex in the DRIFTS measurement.

In addition to these materials, hematite, corundum, mullite, and amorphous silica particles are prepared by spray pyrolysis (13–14) and evaluated for their efficacy in heterogeneous nucleation of ammonium sulfate (8). However, these materials are not studied by DRIFTS in the present work due to the long collection times required to obtain sufficient mass of collected aerosol for DRIFTS measurements. The materials and their efficacies to induce nucleation are included in the epitaxial modeling (vide infra).

Sulfate Coating (DRIFTS). An aliquot of aqueous (NH₄)₂SO₄ is added to the minerals (0.15 g) in a 250 mL beaker. The aliquot volume and concentration (either 26 or 110 mM) are selected to obtain the desired coating thickness of (NH₄)₂SO₄. As a surrogate for thickness, the concentration unit employed throughout this paper is the weight percent (wt %) of (NH₄)₂SO₄ on the mineral, which is calculated by dividing the mass of (NH₄)₂SO₄ in the aqueous volume used by the total mass of the mineral and (NH₄)₂SO₄. For each mineral, (NH₄)₂SO₄ compositions of 2, 5, 10, 15, 20, and 30 wt % are prepared. The mineral and aqueous solution are well-mixed to ensure an even coating of (NH₄)₂SO₄ on all particles, and the beakers are placed in an oven at 105 °C. The oven temperature must be limited to 105 °C to prevent thermal decomposition (15–16). The beakers are left in the oven until the water evaporates and the dry mineral particles with adsorbed (NH₄)₂SO₄ remain.

Infrared Measurement. For a DRIFTS measurement, the sample (5 mg) is ground into an amalgam with a fine KBr powder (5–10 wt % sample) in an agate mortar and pestle. Imprecision in the sample mass (ca. 5 mg) yields DRIFTS spectra of arbitrary signal strength so that a normalization procedure is employed during spectral analysis. The well-mixed powder is spooned into the DRIFTS accessory (Pike Technologies, Madison, WI) sample cup. Excess amalgam is removed by dragging a razor across the top of the sample cup. A Nicolet Magna 560 FTIR is employed to record the spectra from 400 to 4000 cm⁻¹ with 4 cm⁻¹ resolution and averaging 800 scans. Prior to these measurements, a background spectrum is recorded using neat KBr powder. The recorded spectrum is processed by the Kubelka–Munk algorithm to compensate for the lower peak intensities at high wavenumbers and rounded peak shapes of DRIFTS spectra (17). Once converted, the spectra are nominally linear with concentration. In addition to the coated samples, DRIFTS reference spectra are recorded separately for neat (NH₄)₂SO₄(s) and the five minerals. The mineral reference samples are prepared in the same way as the coated samples (vide supra), except that the particles are mixed with Nanopure water instead of aqueous ammonium sulfate solutions.

Spectral Processing. Spectral features resulting from (NH₄)₂SO₄(s) adsorbed to the mineral surface are isolated by subtracting a scaled (NH₄)₂SO₄ reference spectrum and a scaled mineral reference spectrum from the spectrum of the coated mineral. The scaling factors are chosen to remove as completely as possible bulk (NH₄)₂SO₄(s) and mineral, as judged qualitatively by us in an interactive spectral analysis mode with the Nicolet software. Generally, an ammonium residual is unchanged from bulk (NH₄)₂SO₄(s), while the sulfato-stretch is significantly shifted and sometimes split. We denote the metal-sulfato surface complex as >MO₂SO₂²⁻, arising from >MOH + SO₄²⁻ where “>” denotes the underlying crystal lattice and >X is a surface group.

Epitaxial Disregistry Modeling. A mineral particle is a closed form object composed of several crystallographic faces,

each of which is a plausible surface for the heterogeneous nucleation of a (NH₄)₂SO₄(s) germ from a supersaturated aqueous solution. A germ first forms with a specific crystallographic face of (NH₄)₂SO₄(s) abutted to a face of the mineral. For each possible permutation in pairings of the crystallographic faces of (NH₄)₂SO₄(s) and a mineral, an energy interaction term related to the crystallographic misfit (i.e., the disregistry) is calculated based upon the strain necessary to obtain crystallographic match between the two surfaces. Consideration of all the low index surfaces of (NH₄)₂SO₄(s) and the mineral yields a matrix of energy values. For each mineral, the strain energy matrix is obtained, and a correlation with measured heterogeneous nucleation properties (viz. RH for efflorescence) is then established.

The implementation of the model proceeds as follows. First, the atomic coordinates of all minerals are obtained from literature (18–25). Second, the three-dimensional crystallographic structure is obtained and then sectional slices of specific crystal faces are made. We accomplish this effort with *Crystal Office* (Atomic Softtek, Ontario, Canada). Third, the atomic locations of the metal atoms on a specific crystal face and likewise those of sulfate on a specific face of ammonium sulfate are imported into an algorithm in *Mathematica* (Wolfram Research, Champaign, IL). Figure 3 provides an example of the atomic positions of iron atoms on the [001] surface of α-Fe₂O₃ and the sulfate moieties on the [001] surface of (NH₄)₂SO₄. The strain energy associated with each sulfate group is approximated by the classical harmonic oscillator description of atomic interactions, viz. kx^2 where k is the force constant of the bond and x is the nearest iron neighbor to the sulfate (26). (We assume k is principally characteristic of sulfate and remains invariant among sulfate-mineral face pairings.) The total strain energy, E , is the sum across all sulfates and is minimized by translation and rotation of the sulfate face relative to the mineral face. We employ a geometric simplex package for the minimization within *Mathematica* (27). This process is repeated for all crystallographic face pairs. In addition, for comparison among pairs, the strain energy is normalized by the square of the number of sulfate atoms. Evidently, normalization by the number of sulfate atoms is advisable because energy per sulfate is desirable. We normalize by the square as a heuristic method to emphasize those faces having more sulfates. We reason that those faces with few sulfates constitute unlikely precursors to germ formation due to the spatial separation of the adsorbed sulfates, which are the second layer in an atomic template (following the metal atom layer) for germ formation. In the case of a perfect fit, $E = 0$. For values above zero, values of E are on an arbitrary numerical scale set by the numerical value of k , which we have chosen simply as unity since the strain energy is arbitrary in our model treatment. In this regard, $E = 0$ is associated with a classical heterogeneous nucleation compatibility parameter of $m = 1$. For $E > 0$, the functional relationship $m = f(E)$ is not known, though it is certainly monotonic.

Results

DRIFTS spectra of TiO₂-P25, δ-Al₂O₃, α-Fe₂O₃, and monoclinic ZrO₂ coated with (NH₄)₂SO₄(s) are shown in Figure 1. Sulfate and ammonium absorb at 1121 cm⁻¹ (ν_3) and 1400 cm⁻¹ (ν_4), respectively (28). Absorptions below 1000 cm⁻¹ (e.g., sulfate at 612 cm⁻¹) are masked by the minerals (29). The shown spectra are normalized to the strength of the sulfate peak because the absolute signal strength by our experimental methods is arbitrary. At lower loadings, surface structures give rise to a greater fraction of the total absorption. For all oxides, a shoulder is apparent at 70 to 120 cm⁻¹ blue-shifted relative to 1121 cm⁻¹. In the case of TiO₂-P25, a second absorption feature at 1150 cm⁻¹ is apparent at the highest loadings.

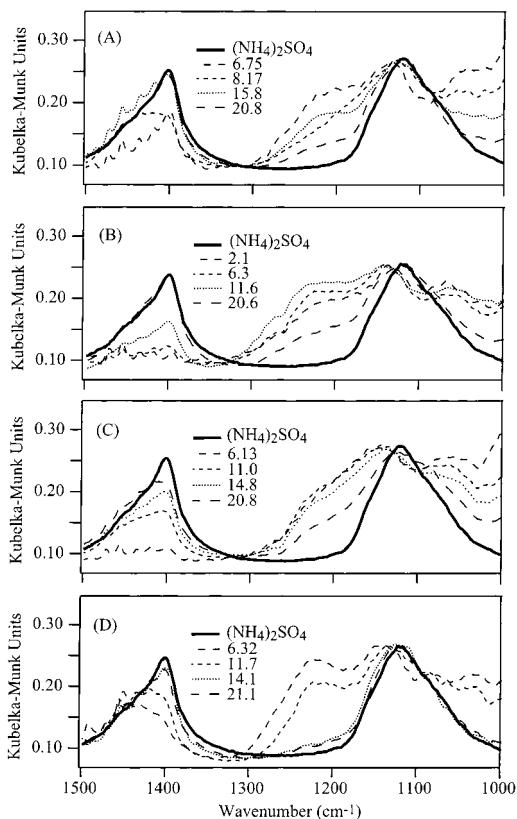


FIGURE 1. DRIFTS spectra of (A) TiO_2 , (B) $\delta\text{-Al}_2\text{O}_3$, (C) $\alpha\text{-Fe}_2\text{O}_3$, and (D) ZrO_2 coated with several $(\text{NH}_4)_2\text{SO}_4(\text{s})$ loadings. The weight percent loadings are indicated in the figure. Spectra are normalized to the strength of the sulfate peak.

The infrared spectrum of the surface adsorbed metal-sulfato structure is obtained by the difference spectra of a scaled $(\text{NH}_4)_2\text{SO}_4(\text{s})$ spectrum and a collected spectrum (Figure 1). The DRIFTS difference spectra are shown in Figure 2 for $\text{TiO}_2\text{-P25}$, $\delta\text{-Al}_2\text{O}_3$, $\alpha\text{-Fe}_2\text{O}_3$, and monoclinic ZrO_2 coated with $(\text{NH}_4)_2\text{SO}_4(\text{s})$. Table 1 summarizes the differences in wavenumber between the surface sulfate peak (as determined from the subtraction spectra) and the reference sulfate peak for each coated mineral. The $\alpha\text{-Fe}_2\text{O}_3$ surface sulfate peak shows the greatest difference at $120 \pm 20 \text{ cm}^{-1}$, followed by monoclinic ZrO_2 , $\text{TiO}_2\text{-P25}$, and $\delta\text{-Al}_2\text{O}_3$. An additional peak occurs at $1150 \pm 20 \text{ cm}^{-1}$ for 20.8 and 30.2 wt % $(\text{NH}_4)_2\text{SO}_4$ with $\text{TiO}_2\text{-P25}$.

Figure 3 shows an example of the optimized registry between the iron atoms on the [001] surface of $\alpha\text{-Fe}_2\text{O}_3$ and the sulfate moieties on the [001] surface of a $(\text{NH}_4)_2\text{SO}_4$ germ. In this example, the sulfate moieties bond to every other atomic layer of iron atoms, and two sulfates bind each iron atom. The unitless strain energy associated with sulfate distortions is 0.05. This value and the other energies values for pairs of ammonium sulfate and hematite faces are shown in Table 2 (Supporting Information). The values for the calculations on the other substrates are given in Tables 3–7 (Supporting Information).

Histograms of optimized unitless strain energies between pairs of faces selected from the $\{(001), (011), (010), (100), (111), (110), (101)\}$ set of $(\text{NH}_4)_2\text{SO}_4$ and $\{(001), (010), (011), (100), (111), (110), (101)\}$ set of the several substrates, including corundum, hematite, mullite, rutile, anatase, and baddeleyite are shown in Figure 4. The histograms for submicron particles (ca. 250 nm) generated by spray pyrolysis and commercially purchased supermicron particles (ca. 2 μm) are separated in Figure 4A,B. On each histogram, the saturation ratio at which aqueous ammonium sulfate is

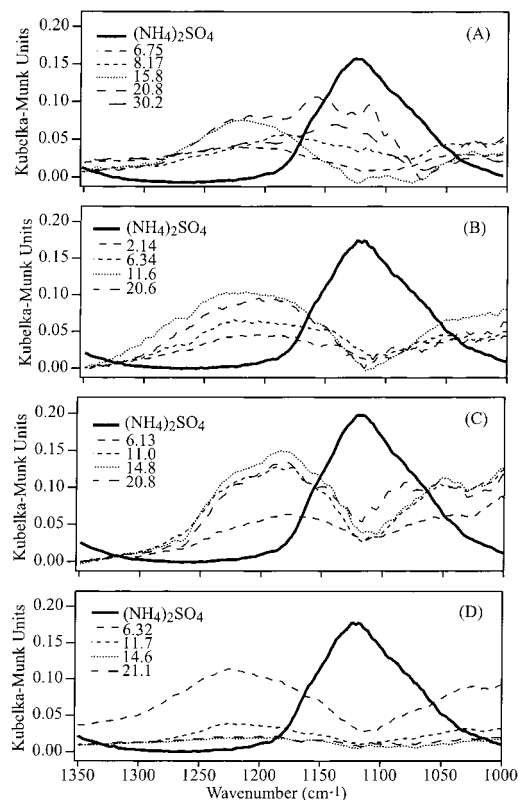


FIGURE 2. Difference spectra obtained by subtracting a scaled $(\text{NH}_4)_2\text{SO}_4(\text{s})$ spectrum from the collected spectra (Figure 1). The residual is the infrared spectra of the sulfato-metal complex. The spectra are (A) TiO_2 , (B) $\delta\text{-Al}_2\text{O}_3$, (C) $\alpha\text{-Fe}_2\text{O}_3$, and (D) ZrO_2 coated with several $(\text{NH}_4)_2\text{SO}_4(\text{s})$ loadings. The weight percent loadings are indicated in the figure.

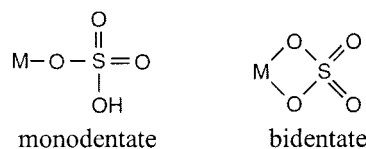
TABLE 1. Wavenumber Shift, $\Delta\tilde{\nu}$ (cm^{-1}), of the Sulfato-Metal Infrared Peak Position Relative to Neat Ammonium Sulfate (1120 cm^{-1})

oxide substrate	$\Delta\tilde{\nu}$ (sulfate) (cm^{-1})	
	peak 1	peak 2
TiO_2	90 ± 30	30 ± 20
Al_2O_3	70 ± 20	
Fe_2O_3	120 ± 20	
ZrO_2	100 ± 30	

observed to rapidly crystallize (7–8) is shown. The upper row of numbers in each figure indicates the strain energy bin while the lower row indicates the number of occurrences. For example, in Figure 4A for corundum, there are 6 pairs of faces of the permutations considered whose strain energies fall between $0.06 \leq E < 0.08$. The reader may verify this fact by an investigation of Table 3.

Discussion

Surface Structures. FTIR studies of aqueous sulfate adsorption to hematite have been conducted (30). Sulfate adsorbs to a mineral surface through either one or two oxygen atoms, making monodentate or bidentate sulfato-metal surface structures possible, as follows:



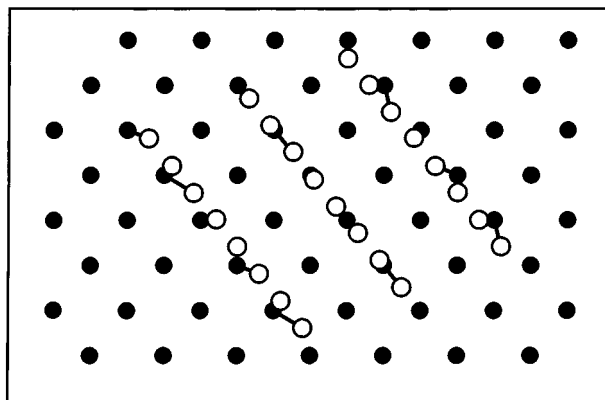


FIGURE 3. The optimized registry between the iron atoms (●) on the [001] surface of α -Fe₂O₃ and the sulfate moieties (○) on the [001] surface of a (NH₄)₂SO₄ germ. Optimization proceeds by translational and rotational operations on the surface array of sulfate moieties until the sum of the squares of the nearest neighbor distances between sulfate and iron is minimized.

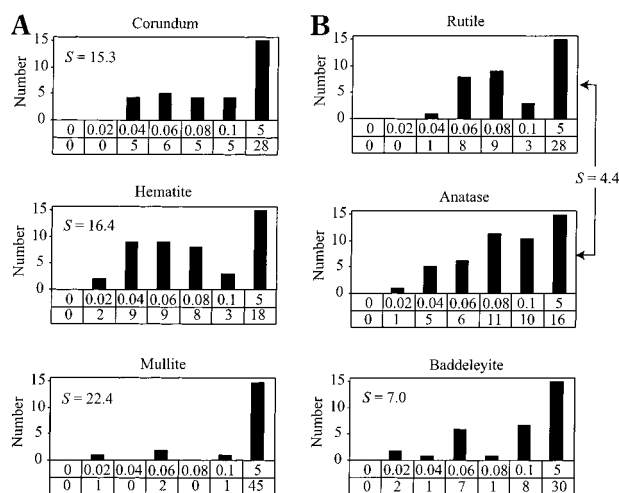


FIGURE 4. Histograms of optimized unitless strain energies between pairs of faces selected from the $\{(001), (011), (010), (100), (111), (110), (101)\}$ set of (NH₄)₂SO₄ and $\{(001), (010), (011), (100), (111), (110), (101)\}$ set of the several substrates, including corundum, hematite, mullite, rutile, anatase, and baddeleyite. Tables 2 through 7 in Supplementary Information contain the data sets from which the histograms are constructed. The saturation ratio, at which value aqueous ammonium sulfate rapidly heterogeneously crystallizes on particles of the several substrates, is shown on each histogram. (A) Particles are submicron (ca. 250 nm) and are generated by spray pyrolysis. (B) Particles are supermicron (ca. 2 μ m) and are purchased commercially and mechanically suspended to form aerosol.

The infrared spectrum of sulfate depends on its symmetry, and the symmetry of the adsorbed sulfate changes depending on whether it is monodentate or bidentate. Free sulfate ion in solution belongs to the T_d point group, in which only the triply degenerate ν_3 and ν_4 vibrational modes are infrared active (31). Only the ν_3 vibrational mode occurs above 1000 cm^{-1} , specifically at 1100 cm^{-1} . The symmetry of the sulfate ion is reduced when it is adsorbed to a surface. A monodentate surface structure results in C_{3v} symmetry, for which the ν_1 vibrational mode becomes active, and the ν_3 and ν_4 vibrational modes each split into two modes (32–33). Thus, for a monodentate surface sulfato-metal complex, two peaks are present above 1000 cm^{-1} due to the splitting of the ν_3 mode. The symmetry of the sulfate ion is further reduced to C_{2v} when it is bound through two oxygen atoms, resulting in bidentate surface structure. For this symmetry, the ν_3 vibrational mode of the sulfate ion splits into three bands.

Thus, for a bidentate surface sulfato-metal complex, three vibrational modes are expected above 1000 cm^{-1} . In contrast, NH₄⁺ does not specifically interact with the mineral surface but rather with the chemisorbed sulfate. The effect is a weaker interaction and minimal distortion from T_d symmetry, as indicated by the absence of distortion in the infrared band.

Spectra of (NH₄)₂SO₄ Coated Minerals. The sulfate coated spectra (Figure 2) in this study show at least two distinguishable peaks above 1000 cm^{-1} . A large shoulder at 1250 cm^{-1} is present on the high wavenumber side of the most intense peak (ca. 1130 cm^{-1}). When this shoulder is considered a separate but overlapping peak, then three peaks are present above 1000 cm^{-1} , and bidentate surface structure can be assigned to the adsorbed sulfate on δ -Al₂O₃, TiO₂-P25, and α -Fe₂O₃. Spectra of monoclinic ZrO₂ coated with (NH₄)₂SO₄ also show two distinguishable peaks at lower wavenumber but have two shoulders on the high wavenumber side of the most intense peak, rather than two. Thus, it is difficult to assign a surface structure to monoclinic ZrO₂ coated with (NH₄)₂SO₄.

Implications for Heterogeneous Nucleation. The classical heterogeneous nucleation rate, j ($\text{cm}^{-2} \text{s}^{-1}$), on a planar and energetically homogeneous surface is described by the following equation (4, 34, 35):

$$j = a \exp \left[\frac{-1}{kT} \frac{(2+m)(1-m)^2}{4} \Delta G_{\text{germ}} + \Delta G_{\text{diffusion}} \right] \quad (1)$$

where m is the compatibility parameter, a is the preexponential factor, ΔG_{germ} is the free energy barrier of germ formation, and $\Delta G_{\text{diffusion}}$ is the free energy barrier for atomic jumps across the interface from the aqueous solution to the crystalline germ. The values of a , ΔG_{germ} , and $\Delta G_{\text{diffusion}}$ depend on the aqueous (NH₄)₂SO₄ concentration, but they are independent of the nature of the heterogeneous nucleus. In contrast, m depends on the nature of interaction between ammonium sulfate and the heterogeneous nucleus (i.e., δ -Al₂O₃, monoclinic ZrO₂, TiO₂-P25, or α -Fe₂O₃).

One factor in the nature of a heterogeneous nucleus is its surface acidity. The more acidic the surface, the more readily it will accept negative charge, such as sulfate. Thus, it could be expected that the more acidic the surface, the more efficient the heterogeneous nucleus. The pH values for zero point charge (pH_{zpc}) for Al₂O₃, Fe₂O₃, ZrO₂, and TiO₂ are 8.7, 8.5, 6.4, and 6.25, respectively (36). On the basis of this property alone, sulfate will adsorb most strongly to TiO₂-P25, followed by monoclinic ZrO₂, α -Fe₂O₃, and δ -Al₂O₃. It might be expected that the mineral to which sulfate most strongly adsorbs would show the largest wavenumber shift due to the relocation of electron density. However, the data presented in Table 1 do not support this conclusion. Although δ -Al₂O₃ shows the smallest wavenumber shift, α -Fe₂O₃, which should show only a slightly greater shift than δ -Al₂O₃, actually shows the largest wavenumber shift. Wavenumber shifts do not correspond to the trend in surface acidity of the five minerals, suggesting that the interaction between sulfate and mineral surface is complicated and that factors in addition to surface acidity should be taken into account.

Epitaxial Matching. Within a size class and for the limited number of samples studied, epitaxial matching appears to be an indicator of heterogeneous nucleation activity. As shown in Figure 4A, corundum and hematite have qualitatively similar histograms and efficacies to induce heterogeneous nucleation of aqueous ammonium sulfate (i.e., similar S values). In contrast, mullite is a significantly poorer heterogeneous nucleus and also shows a histogram devoid of many low energy epitaxial fits. In another size class, rutile/anatase of TiO₂-P25 have both more efficient capacities of heterogeneous nucleation as well as better qualitative epitaxial fits, as compared to baddeleyite. It would be

desirable to test this work further against δ -Al₂O₃ ($S = 8.2$), but the atomic assignments necessary for calculating epitaxial energies are not available in existing crystallographic literature, as reviewed by Levin and Brandon (24). In addition, though our initial work is promising in indicating trends between epitaxial matching and heterogeneous activity for two size classes, continued work is advisable in this area before a strong thesis is formed since we have a number of model simplifications (vide infra). The effect of particle size on heterogeneous nucleation efficacy is discussed in more detail in Martin et al. (8). Although atmospheric particles are closed form objects of many crystal faces, it would be desirable in a laboratory setting to studying single crystalline faces in a series to test their relative nucleation efficiencies in line with those anticipated from the calculations shown in Tables 2 through 7 (Supporting Information). We also studied amorphous silica particles and found no difference between their ability to induce crystallization of aqueous ammonium sulfate and homogeneous nucleation (i.e., $S = 35$ in both cases); an amorphous surface provides no template for epitaxial matching with an incipient germ.

The epitaxial matching in Figure 3 shows the incipient chemisorbed germ is highly ordered. Sulfate binds to every other row of iron atoms, and there are usually two sulfate moieties bound to each iron atom. If this picture is physically realistic, then each sulfate moiety must be bound in a monodentate structure to surficial iron atoms at the moment of critical germ formation. In contrast, the IR spectroscopy indicates bidentate surface structures. We can then understand why the spectroscopic results are not a good indicator of heterogeneous nucleation activity. The surface configuration between the aqueous solution and the underlying substrate at the moment of critical germ formation, as depicted in Figure 3, is much different from the final surface configuration after crystallization and drying, which the DRIFTS measurements indicate are bidentate surface structures.

We can consider the extrapolation of our work to more general atmospheric mineralogy. Hematite and corundum are both of the "corundum" structure type, which means the atoms are located in roughly the same relative positions and in the same absolute positions when unit cell parameters are similar. As such, they show similar histograms (Figure 4A) for epitaxial strain energies. As a working idea, we would preliminarily suggest this similar strain energy explains their similar efficacies as substrates of heterogeneous nucleation (i.e., $S = 15.3$ and 16.4). By this line of reasoning, we can then extend this structure-activity relationship to minerals we have not studied that are of similar structure type and unit cell parameters. We conclude that hematite, corundum, eskolaite (Cr₂O₃), and karelianite (V₂O₃) particles of similar size may have similar efficacies as heterogeneous nuclei for the crystallization of aqueous ammonium sulfate. In addition, if we assume sulfate binds indiscriminately to metals ions, then certain mixed minerals reduce to the corundum structure, including ilmenite (FeTiO₃) and pyrophanite (MnTiO₃). We similarly group cassiterite (SnO₂) and pyrolusite (MnO₂) with the rutile we studied. If borne out in further work, this approach has the potential to reduce the question of heterogeneous nucleation inside atmospheric aqueous electrolytes from the full complexity of atmospheric mineralogy to the slightly smaller question of structural types and particle sizes.

Simplifications in our epitaxial modeling include a reduction of the crystal matching problem to two-dimensions; consideration of only sulfate distortion; the permission of spatial coincidence of two or more sulfates on the same metal atom; a classical isotropic harmonic oscillator energy interaction; reconstruction of only the first layer of sulfate atoms; an absence of the consideration of hydroxylation of

the mineral surfaces and other surface reconstructions and defects; and the existence of all low order surfaces on a specific mineral three-dimensional form (i.e., a particle). In addition, we treat the nucleation event as a spherical-cap germ with a specific crystallographic face of (NH₄)₂SO₄(s) abutted to one of the faces of the mineral. Although a solid-germ is idealized by a Wulff construction rather than a spherical-cap, possible contributions from anisotropic surface tensions are omitted in our model. Of the many factors contributing to the activation energy, our hypothesis is that a single interaction term between germ and substrate (as formulated in classical heterogeneous nucleation theory by the compatibility parameter) dominates the overall nucleation rate.

Acknowledgments

We are grateful for support received from the NSF Atmospheric Chemistry Program and a Presidential Early Career Award in Science and Engineering (PECASE). J. Schlenker received support to do undergraduate research as an educational outreach activity of the NSF CAREER program. O. Duckworth was funded by a United States Environmental Protection Agency Science to Achieve Results (USEPA STAR) Fellowship.

Supporting Information Available

Tables of goodness of atomic fit between unreconstructed faces of six minerals and ammonium sulfate. Table entries are the unitless strain energies associated with atomic translation for matching between the positions of sulfate moieties and surficial metal atoms. This material is available free of charge via the Internet at <http://pubs.acs.org>.

Literature Cited

- (1) IPCC. In *Climate Change 1995*; Cambridge University Press: New York, 1996.
- (2) IPCC. In *Climate Change 1994*; Cambridge University Press: New York, 1995.
- (3) Seinfeld, J. *National Research Council, Panel on Aerosol Radiative Forcing and Climate Change. A Plan for a Research Program on Aerosol Radiative Forcing and Climate Change*; National Academy Press: Washington, DC, 1996.
- (4) Pruppacher, H. R.; Klett, J. D. *Microphysics of Clouds and Precipitation*; Kluwer: Dordrecht, 1997.
- (5) Warneck, P. *Chemistry of the Natural Atmosphere*; Academic Press: San Diego, 1999.
- (6) Martin, S. T. *Chem. Rev.* **2000**, *100*, 3403.
- (7) Han, J.; Martin, S. T. *J. Geophys. Res.* **1999**, *104*, 3543.
- (8) Martin, S. T.; Han, J. H.; Hung, H. M. *Geophys. Res. Lett.* **2001**, submitted.
- (9) Griffiths, P. R.; De Haseth, J. A. *Fourier Transform Infrared Spectrometry*; Wiley: New York, 1986.
- (10) Stumm, W. *Chemistry of the Solid-Water Interface*; Wiley: New York, 1992.
- (11) Hillier, A. C.; Ward, M. D. *Phys. Rev. B* **1996**, *54*, 14037–14051.
- (12) *Degussa Technol. Bull. Pigments* **1990**, *56*, Degussa Corp., Akron, Ohio.
- (13) Martin, S. T.; Yu, J.; Han, J. H.; Verdier, M.; Li, J.; Buseck, P. R. *J. Aerosol Sci.* **2000**, *31*, 1283.
- (14) Martin, S. T.; Han, J. H. *J. Crystal Growth* **2000**, *219*, 290.
- (15) Halstead, W. D. *J. Appl. Chem.* **1970**, *20*, 129.
- (16) Kiyoura, R.; Urano, K. *Ind. Eng. Chem. Process. Des. Develop.* **1970**, *9*, 489.
- (17) Kubelka, P. *J. Opt. Soc. Am.* **1948**, *38*, 448.
- (18) Newnham, R. E.; De Haan, Y. M. *Z. Krist.* **1962**, *117*, 235.
- (19) Blake, R. L.; Hessevick, R. E. *Am. Mineral.* **1966**, *51*, 123.
- (20) Ban, T.; Okada, K. *J. Am. Ceram. Soc.* **1992**, *75*, 227.
- (21) Shintani, H.; Sato, S.; Saito, Y. *Acta Crystallogr.* **1975**, *B31*, 1981.
- (22) Horn, M. C.; Schwerdtfeger, C. F.; Meagher, E. P. *Z. Kristallogr.* **1972**, *136*, 273.
- (23) Smith, D. K.; Newkirk, H. W. *Acta Crystallogr.* **1965**, *18*, 983.
- (24) Levin, I.; Brandon, D. *J. Am. Ceram. Soc.* **1998**, *81*, 1995.
- (25) Wyckoff, R. W. G. *Crystal Structures*; Interscience: New York, 1963; Vol. 3.
- (26) McQuarrie, D. A. *Quantum Chemistry*; University Science Books: Mill Valley, CA, 1983.

- (27) Carley, A. F.; Morgan, P. H. *Computational Methods in the Chemical Sciences*; Wiley: New York, 1989.
- (28) Nakamoto, K. *Infrared and Raman Spectra of Inorganic and Coordination Compounds*; 4th ed.; John Wiley & Sons: New York, 1986.
- (29) Williams, Q. In *Mineral Physics & Crystallography*; Ahrens, T. J., Ed.; American Geophysical Union: Washington, DC, 1995.
- (30) Hug, S. J. *J. Colloid Interface Sci.* **1997**, *188*, 415.
- (31) Steger, E.; Schmidts, W. *Ber. Bunsenges. J. Phys. Chem.* **1964**, *68*, 102.
- (32) Nart, F. C.; Iwasita, T. *J. Electroanal. Chem.* **1991**, *308*, 277.
- (33) Nart, F. C.; Iwasita, T. *J. Electroanal. Chem.* **1992**, *322*, 289.
- (34) *Handbook of Crystal Growth*; Hurle, D. T. J., Ed.; Elsevier: Amsterdam, 1993; Vol. 1a.
- (35) Markov, I. V. *Crystal Growth for Beginners*; World Scientific: Singapore, 1995.
- (36) Stumm, W.; Morgan, J. J. *Aquatic Chemistry*; Wiley: New York, 1996.

Received for review July 28, 2000. Revised manuscript received January 24, 2001. Accepted January 31, 2001.

ES001535V